

Fundamental difference between the two Hall thruster variants

E. Y. Choueiri

Electric Propulsion and Plasma Dynamics Laboratory, Princeton University, Princeton, New Jersey 08544

(Received 16 July 2001; accepted 14 August 2001)

The fundamental difference between the two variants of Hall thrusters, the stationary plasma thruster (SPT) and the thruster with anode layer (TAL), is illustrated quantitatively using an analytical model that accounts for the effects of secondary electron emission (SEE) from the walls. The model includes a prescription for the quenching of the temperature of the electrons on their way to the anode which results from the enhanced electron energy losses to the wall that occur at, and upstream of, an axial location where the wall potential reverses from electron attracting to electron repellent. For the higher SEE coefficient of an insulator wall (compared to that of a metallic one) this sign reversal occurs at a lower electron temperature and is shown to lead to a more extended acceleration region due to the resulting relaxation of the potential gradient required to balance the electron pressure gradient. By replacing the boron nitride walls (SPT) of an idealized Hall thruster with stainless steel (TAL), the acceleration zone is shown analytically to collapse to a region near the anode having an extent that is about eight times smaller than that for the SPT. The results are used to construct a detailed phenomenological picture of the fundamental difference between the two Hall thruster variants. © 2001 American Institute of Physics. [DOI: 10.1063/1.1409344]

I. INTRODUCTION

A. Historical perspective

Historically, the Hall thruster derived, in the early 1960s, from ongoing work on magnetrons and other cross-field plasma sources. The earliest published description of a Hall accelerator that considerably resembles its modern progenies is in a series of brief communications by Seikel and Reshotko, and Salz, Lary, and co-workers in the 1962 Bulletin of the American Physical Society.¹⁻³ At this early date in its history, the device was simply called a Hall current ion accelerator and was recognized for its promise as a high-specific-impulse thruster for spacecraft propulsion. A series of publications, all in the US, followed, including seminal work that described the device's operational characteristics⁴ (1964), explored the use of alkali-metal propellant^{5,6} (1964,1965), and studied the governing physical processes^{7,8} (1966). By that time, the device had many of the features presently possessed by its modern counterpart, whose properties, underlying physical mechanisms, and operational characteristics were more recently described in Refs. 9 and 10.

The earliest related Soviet experimental work¹¹ reported in international journals dates to 1968. Since around that time, the device, which was largely neglected in the US in favor of ion thrusters, was the subject of considerable research and development effort in the Soviet Union which led to its use on numerous Soviet spacecraft.¹² The most successful "commercial" version of the device is often called "stationary plasma thruster," or SPT, in the translated Russian literature. Although this name is not very descriptive (it probably stems from a need to differentiate it from *pulsed* plasma thrusters) it has been commonly adopted by default in the West where a substantial resurgence in interest¹³ in Hall thrusters started in the early 1990s.

It is relevant to our discussion to note that the channel walls of the SPT, shown in Fig. 1, are always made of insulator material, which is typically boron nitride. Another variant of Hall thrusters, to be differentiated from the SPT, has metallic walls and a considerably shorter channel.

This second variant also originated in the US and can be traced back to the work of Meyer¹⁴⁻¹⁷ (1966) who, using a device similar to the standard Hall thruster, discovered a qualitatively different potential structure through which the ions are accelerated in a relatively thin layer at the anode. Due to the small spatial extent of the acceleration region, the discharge does not need to be contained in a long channel and consequently, its originator claimed that it had substantially less wall losses than the standard Hall thruster.

The fate of this variant is similar to that of the SPT, in that it was further developed almost exclusively in the Soviet Union where, starting in the early to 1970s, it has acquired its own group of proponents who claim¹⁸ it has advantages over the SPT. Again, the translated Russian literature gave us another awkward appellation, which in the case of this variant is "thruster with anode layer" or TAL. Of relevance to our discussion is the fact that the TAL always has metallic walls.

Aside from the different wall material, the substantially shorter effective acceleration region (confined to a potential drop in a thin layer at the anode whose axial extent is on the order of the electron cyclotron radius) the TAL, in comparison to the SPT operated with similar conditions, typically has a significantly higher electron temperature (see Ref. 9 for instance).

B. Motivation and scope

Both Hall thruster variants exist today and both have attained technological maturity and space worthiness as

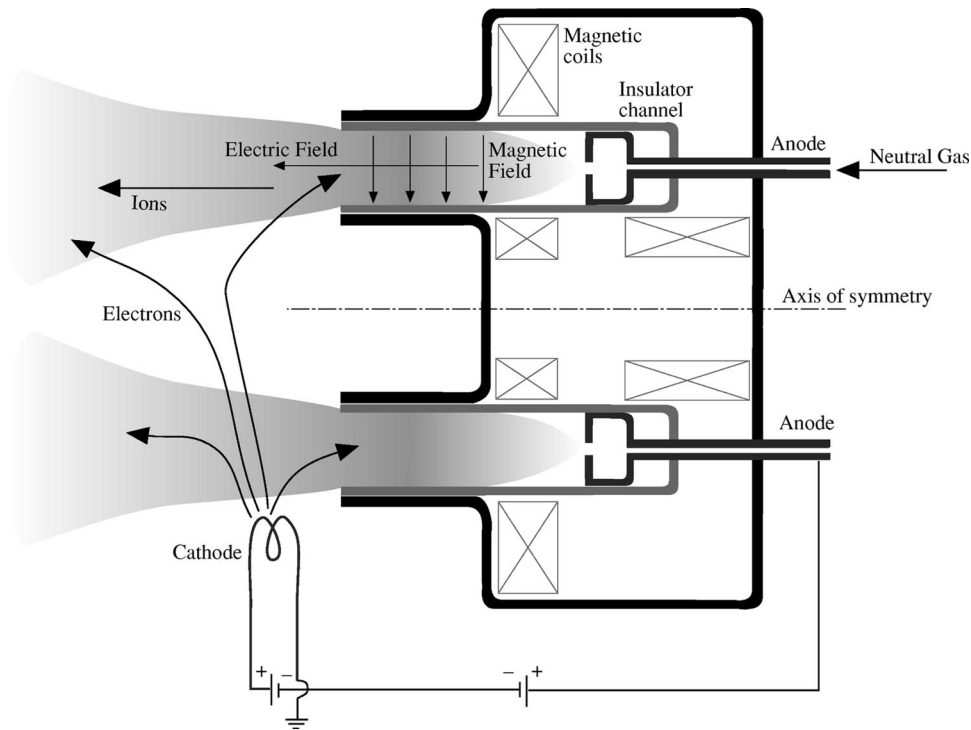


FIG. 1. Schematic of a Hall thruster with an extended insulator channel (SPT) showing the external cathode, the internal anode, the radial magnetic field, and typical particle trajectories.

spacecraft thrusters. The scope of this paper is not to fully describe and contrast these two types of thrusters, or to evaluate the claimed advantages of each, but rather to answer the following basic questions:

- (1) Why does the introduction of a metallic wall into a discharge of this kind result in a substantial decrease in the spatial extent of the accelerating layer with respect to the case with insulator walls?
- (2) To what extent does the ion acceleration in each variant happen in a quasineutral region as opposed to a space-charge-limited one?
- (3) Can one use an analytical model to construct a clear picture of the processes that underlie the fundamental difference between these two Hall thruster variants?

While a wide literature exists for each of these devices, a discussion of the above-mentioned questions in a *comparative* context appears to be lacking.

In that direction, we set our primary goal in Sec. II to be the formulation of a model for the axial extent of the effective acceleration region as a function of the wall properties. We do so by making simplifying assumptions that allow us, as much as possible, to keep the formulation tractable analytically without losing the salient physics controlling the extent of the acceleration region. In Sec. III we seek solutions for the analytical model and discuss the validity of the approximation that allows us to obtain such solutions. This is followed by a discussion of the physical implications of the results. We conclude in Sec. IV with a detailed phenomenological picture drawn from the results of the preceding sections.

II. THEORETICAL MODEL

We should state at the outset that the aim of the model is not to predict the measured performance or detailed properties of Hall thrusters but rather to answer the three questions posed in Sec. I.

Since our goal is to arrive at a description of the axial extent of the effective acceleration region as a function of the wall properties, we need to relate the electrostatics of the problem to the relevant wall effects.

A. Analytical formulation

We adopt the rectangular coordinate system shown schematically in Fig. 2. The x axis is along the thruster axis (i.e., along the applied electric field E_x) and the z axis is along the thruster radius, i.e., along the radial magnetic field B_r which is taken to be constant and uniform. The y axis therefore

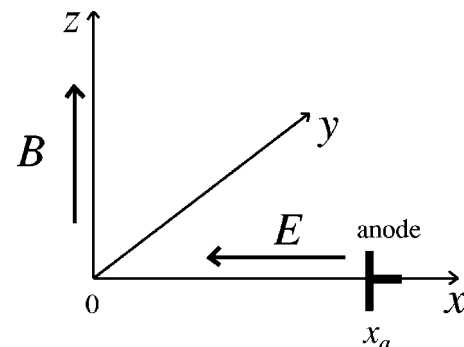


FIG. 2. Adopted rectangular coordinate system. The coordinate x_a represents the position of the anode with respect to the downstream end of the acceleration region which is placed at the origin.

corresponds to the azimuthal (Hall) dimension. The coordinate x_a represents the position of the anode with respect to the downstream end of the acceleration region which is placed at the origin. The coordinate x_a , therefore, becomes a measure of the extent of the acceleration region. Our goal is to estimate x_a as a function of the wall properties.

B. Governing equations

Zharinov and Popov¹⁹ modeled the potential profile in an idealized $\mathbf{E} \times \mathbf{B}$ discharge but were not concerned with the walls and their effects. We adopt their formulation as a starting point and evolve it to explicitly include the relevant wall effects.

We start by writing the following momentum balance for the electrons in the x direction:

$$\nu_e n_e v_e m_e + e n_e E + (\mathbf{j}_e \times \mathbf{B})_x + \frac{dP_e}{dx} = 0, \quad (1)$$

where the electron inertia in the cross-field direction is taken as negligible. Here $\mathbf{j}_e = e n_e \mathbf{v}_e$ is the electron current density, ν_e is the electron collision frequency, and the rest of the symbols have their usual meaning.

By using the following relations:

$$(\mathbf{j}_e \times \mathbf{B})_x = j_{e_y} B = j_{e_x} B \Omega_e, \quad E_x = -\frac{d\phi}{dx}, \quad (2)$$

where $\Omega_e \equiv \nu_e / \omega_{ce}$ is the electron Hall parameter, and ϕ is the potential, Eq. (1) can be solved for j_{e_x} ,

$$j_{e_x} = \mu_{e\perp} \left[e n_e \frac{d\phi}{dx} - \frac{d(n_e T_e)}{dx} \right], \quad (3)$$

where $\mu_{e\perp}$ is the classical cross-field (Pedersen) electron mobility

$$\mu_{e\perp} = \frac{e}{m_e \nu_e} \frac{1}{1 + \Omega_e^2}. \quad (4)$$

In Eq. (3) we have explicitly expressed the electron pressure as $n_e T_e$, where the electron temperature is in units of energy.

We also need to write a continuity equation for the electrons

$$\nabla \cdot \mathbf{j} = \nu_{iz} e n_e, \quad (5)$$

where ν_{iz} is the ionization frequency. Explicitly we have

$$\frac{\partial j_{e_x}}{\partial x} + \frac{\partial j_{e_y}}{\partial y} + \frac{\partial j_{e_z}}{\partial z} = \nu_{iz} e n_e. \quad (6)$$

The second term vanishes if we assume uniformity in the y direction. We will also assume that, as far as the electrodynamics are concerned, no current flows along the magnetic field. We are therefore left with

$$\frac{d j_{e_x}}{dx} = \nu_{iz} e n_e. \quad (7)$$

Here ν_{iz} is the frequency of ionization which, in Hall thrusters, is due to electron impact.

Unlike in Ref. 19 we shall not be concerned with Poisson's equation since we will focus our analysis on the

quasineutral part of the acceleration region which, as we shall see, gives a good measure of the spatial extent of the accelerating potential. [We will later show how a general solution for the nonquasineutral (sheath) part of the potential drop can be adapted to complement our quasineutral solutions.] Therefore, we take $n_e = n_i$. Furthermore, like in that reference, we shall neglect the contribution of ion production to the ion continuity relation. This approximation becomes justified when the the pressure is low and when the ion current significantly exceeds the electron current (which is the case in an efficient Hall thruster). Therefore $j_i = e n_i v_i = \text{constant}$. We shall take this constant to be j_{i_0} representing the ion current at the exit (which is the downstream end of the acceleration region and is located at the origin of the coordinate system shown in Fig. 2). We can thus write

$$n_e = n_i = \frac{j_i}{e_i v_i} \approx \frac{j_{i_0}}{e_i v_i} = \frac{j_{i_0}}{e \left[\frac{2e(\phi_a - \phi)}{M} \right]^{1/2}}, \quad (8)$$

where ϕ_a is the anode potential with respect to that at the downstream end of the acceleration zone. The latter potential is taken to be zero.

We shall, for the sake of analytical tractability, take ν_e , ν_{iz} , and $\nu_{e\perp}$ to be constant parameters of the problem. Furthermore we assume $\Omega_e \gg 1$, which is justifiable for a Hall thruster. All that remains in order to close the system of equations [Eqs. (3), (7), and (8)], is an energy equation or a prescription of the electron temperature in terms of the potential, i.e., $T_e(\phi)$.

In Ref. 19, the authors adopt the following ultrasimplified energy equation:

$$\frac{kT_e}{e} = \beta \phi, \quad (9)$$

where β is a number between 0 and 1. This means that the electron energy is allowed to increase linearly with the potential as the electrons move from the cathode (at the downstream end of the acceleration region) to the anode. We will improve on this prescription by adopting a more physical, albeit more complicated, form for $T_e(\phi)$ that would allow us to introduce the wall properties and their effects into the problem.

C. Prescription for $T_e(\phi)$ including wall properties

The wall properties we shall be concerned with here are those related to the secondary electron emission (SEE) characteristics of the walls. When plasma (primary) electrons impact the walls, a flux of *low-energy* secondary electrons are emitted whose magnitude depends on the SEE coefficient, γ , defined as the ratio of the number of secondary electrons to that of the primaries.²⁰⁻²²

SEE in Hall thrusters has been considered before in the context of the near-wall conductivity effect which has been proposed by Morozov *et al.*²³ to explain the well-known enhancement in cross-field electron mobility. The most explicit model for the effect has been advanced by Fife *et al.*,²⁴ who incorporated a model for near-wall conductivity in their nu-

merical study of low-frequency oscillations in Hall thrusters. We shall not be concerned here with the near-wall conductivity effect but rather with the SEE effects on the electron temperature. By imposing a no-current condition at the walls and accounting for the fluxes of ions, primary and secondary electrons, the wall potential, ϕ_w , can be written as²⁴

$$\phi_w = \frac{-T_e}{e} \ln \left[(1 - \gamma_{\text{eff}}) e^{1/2} \frac{\bar{C}_e}{4v_B} \right], \quad (10)$$

where the symbol e inside the square brackets represents the base of the natural logarithm (and not the electron charge), $\bar{C}_e \equiv (8T_e/\pi m_e)^{1/2}$ is the electron average speed, $v_B \equiv (T_e/M)^{1/2}$ is the standard Bohm velocity, and γ_{eff} is the effective SEE coefficient given by

$$\gamma_{\text{eff}} = \Gamma(2+b) a T_e^b. \quad (11)$$

Here $\Gamma(c)$ is the gamma function and a and b are the parameters of the exponential fit

$$\gamma \approx a \epsilon^b \quad (12)$$

to the experimental data of the measured dependence of γ on the energy of primary electrons, ϵ , in eV. Such a measurement, luckily, has been reported in Ref. 25 for the case of boron nitride, which is commonly the wall material for the SPT. The corresponding values^{24,25} are (for $\epsilon < 30$ eV)

$$a = 0.141, \quad b = 0.567 \quad (\text{boron nitride}). \quad (13)$$

For stainless steel walls we use the data from Ref. 26, which yield

$$a = 0.04, \quad b = 0.61 \quad (\text{stainless steel}). \quad (14)$$

There is therefore a substantial difference in the SEE wall properties between the SPT and the TAL. Compared to insulators, metals have a considerably lower γ since the secondary electrons lose their energy rapidly by electron–electron scattering and, as a result, the escape depth is of the order of nanometers at most. Hence γ is typically well below 2 and the energy of the secondaries is low (a few eV).

Most relevant to our discussion is the fact that the sign of the wall potential given by Eq. (10) can change depending on T_e and the SEE parameters a and b . According to Eq. (10) this important sign reversal occurs at a critical electron temperature, T_e^* , given by

$$T_e^* = \left[\frac{1 - \left(\frac{2\pi m_e}{e M} \right)^{1/2}}{a \Gamma(2+b)} \right]^{1/b}. \quad (15)$$

For the SPT and TAL operated with xenon ($M = 131.3$ amu) we therefore have

$$T_{e\text{BN}}^* = 16.5 \text{ eV}, \quad T_{e\text{SS}}^* = 107 \text{ eV}, \quad (16)$$

respectively.

Below T_e^* the wall potential is electron repellent (due to a dearth of secondary electrons) and above it is attractive (to compensate for the enhanced presence of secondaries). This would lead, as indeed has been shown numerically,²⁴ to severe consequences on the magnitude of the electron heat flux to the walls which is negligible for $T_e < T_e^*$ but abruptly

increases for $T_e > T_e^*$. Once T_e^* is exceeded, the large electron heat flux to the walls acts to “short-circuit” any further increase in T_e since the walls now act as a large energy sink. Consequently, and in the spirit of idealization, we limit the electron temperature to T_e^* after this condition is reached at some point on the potential profile.

Based on the previous discussion we are compelled to formulate a model for $T_e(\phi)$ that would replace the simplistic prescription in Eq. (9) with one that includes this SEE-induced quenching effect; specifically, we write

$$T_e = T_e^* (1 - e^{-e\phi/T_e^*}). \quad (17)$$

Now, the energy of the electrons on their way to the anode is allowed, as before, to increase linearly with the potential but is quickly limited to T_e^* for $\phi \geq T_e^*$.

This model explicitly introduces SEE effects to our formulation and, in combination with Eqs. (3), (7), and (8), allows us to study the effects of the walls on the extent of the acceleration zone.

III. SOLUTION

A. Nondimensionalization

Before we proceed with solving the equations it is helpful to nondimensionalize them. In order to provide a link between our results and those of Ref. 19, we adopt the same nondimensionalization:

$$\bar{\phi} \equiv \frac{\phi}{\phi_a}, \quad \bar{x} \equiv \frac{x}{l'}, \quad \bar{n}_e \equiv \frac{n_e}{n'}, \quad (18)$$

and

$$\bar{j}_{e_x} \equiv \frac{j_{e_x}}{j'}, \quad \bar{T}_e \equiv \frac{T_e}{e\phi_a}, \quad (19)$$

where we have used the characteristic length l' , density n' , and current density j' . These reference quantities are defined as follows. The characteristic length, l' , is taken as

$$l' \equiv \left[\frac{e\phi_a}{\frac{v_{iz}}{v_e} m_e \omega_{ce}^2} \right]^{1/2}, \quad (20)$$

where it can be seen that the terms on the right-hand side can be grouped, to a multiplicative constant $\sqrt{v_e/2v_{iz}}$, as a ratio of an electron velocity $(2e\phi_a/m_e)^{1/2}$ to the cyclotron frequency ω_{ce} , which represents an electron cyclotron radius. Hence,

$$l' = \sqrt{\frac{v_e}{2v_{iz}}} r_{ce}. \quad (21)$$

The ratio $v_e/2v_{iz}$ represents an ionization efficiency index (the number of total electron collisions before an ionizing one occurs) and depends on the scaling of the relevant cross sections with T_e . For xenon, as we shall more explicitly quote later, this ratio ranges between unity (at energies exceeding 100 eV) and about 30 (at energies of about 15 eV). Therefore, for our problem, l' is of the same order of mag-

nitude as r_{ce} evaluated at $T_e = \phi_a$, which is an upper bound for the range of r_{ce} values attainable in the device. The characteristic density is

$$n' \equiv \frac{j_{i0}}{e \sqrt{\frac{2e}{M} \phi_a}}, \tag{22}$$

and the characteristic current density j' is given by

$$j' = e v_{iz} n' l'. \tag{23}$$

Under the above-stated assumptions and definitions we obtain the following nondimensional version of Eqs. (3), (7), (8), and (17):

$$\bar{j}_{e_x} = \bar{n}_e \frac{d\bar{\phi}}{d\bar{x}} - \frac{d}{d\bar{x}}(\bar{n}_e \bar{T}_e), \tag{24}$$

$$\frac{d\bar{j}_{e_x}}{d\bar{x}} = \bar{n}_e, \tag{25}$$

$$\bar{n}_e = (1 - \bar{\phi})^{-1/2}, \tag{26}$$

$$\bar{T}_e = \bar{T}_e^* (1 - e^{-\bar{\phi}/\bar{T}_e^*}). \tag{27}$$

We now differentiate Eq. (24) with respect to \bar{x} , equate the result to \bar{n}_e [Eq. (25)], then use the last two equations to eliminate \bar{n}_e and \bar{T}_e . We find after some algebra,

$$\frac{d^2}{d\bar{x}^2} \left[2(1 - \bar{\phi})^{1/2} + \frac{\bar{T}_e^* (1 - e^{-\bar{\phi}/\bar{T}_e^*})}{(1 - \bar{\phi})^{1/2}} \right] + (1 - \bar{\phi})^{-1/2} = 0, \tag{28}$$

which is a second-order nonlinear ordinary differential equation (ODE) in $\bar{\phi}$ subject to the following boundary conditions:

$$\frac{d\bar{\phi}}{d\bar{x}} = 0, \quad \bar{\phi} = 0 \quad \text{at} \quad \bar{x} = 0. \tag{29}$$

Since $\bar{\phi} = 0$ at the location $\bar{x} = 0$, which defines the downstream end of the acceleration zone, and $\bar{\phi} = \bar{\phi}_a = 1$ at \bar{x}_a , which denotes the location of the anode, the extent of the acceleration region is, by definition, \bar{x}_a . Our goal is to solve the above-mentioned differential equation in order to estimate \bar{x}_a for conditions typical of the SPT and TAL.

B. Analytical solutions

Before we attempt to solve Eq. (28) it is instructive to note that, as was the case for the simpler problem treated in Ref. 19, the solution to this equation (which is a quasineutral solution) may not exist over the entire extent of the acceleration region $0 \leq \bar{x} \leq \bar{x}_a$. Indeed, by simply differentiating Eq. (24) once with respect to \bar{x} and factoring the electric field $d\bar{\phi}/d\bar{x}$, we find

$$\bar{j}_{e_x} = \left[\frac{2 - \bar{T}_e^* (1 - e^{-\bar{\phi}/\bar{T}_e^*}) / (1 - \bar{\phi}) - 2e^{-\bar{\phi}/\bar{T}_e^*}}{2(1 - \bar{\phi})^{1/2}} \right] \frac{d\bar{\phi}}{d\bar{x}} \tag{30}$$

and see that the term inside the square bracket vanishes when the potential reaches a critical value, $\bar{\phi}_{qn}$ given by

$$\bar{\phi}_{qn} = 1 - \frac{\bar{T}_e^*}{2}. \tag{31}$$

Since the current \bar{j}_{e_x} must be conducted to the anode and cannot vanish, the first and second derivatives of $\bar{\phi}$ must go to infinity. At the location \bar{x}_{qn} corresponding to this potential, quasineutrality is lost and no solutions of the (quasineutral) governing equation, Eq. (28), exist for $\bar{x} \geq \bar{x}_{qn}$. The solution of Eq. (28), therefore, cannot be used to estimate \bar{x}_a (except for the particular case of $\bar{T}_e^* = 0$ where, as we shall see shortly, a quasineutral solution exists over the entire acceleration zone) but rather \bar{x}_{qn} , which is the axial extent of the *quasineutral part* of the acceleration region. We will shortly show, however, that for typical parameters of the SPT and TAL the distance $\bar{x}_a - \bar{x}_{qn}$, which represents the axial extent of the nonquasineutral sheath on the anode, is small enough, when compared to \bar{x}_a , that we can approximately estimate the extent of the actual acceleration region by \bar{x}_{qn} as obtained from the solution of Eq. (28).

We now turn our attention to the task of finding an analytical solution for this equation and note that, unlike the simpler case studied in Ref. 19, there is no apparent transformation that can be used to transform this nonlinear ODE into an integrable one. This is due to the presence of the function

$$F_1(\bar{\phi}) = \frac{(1 - e^{-\bar{\phi}/\bar{T}_e^*})}{(1 - \bar{\phi})^{1/2}} \tag{32}$$

inside the square brackets of Eq. (28). If, however, we approximate this function by

$$F_2(\bar{\phi}) = \frac{1}{(1 - \bar{\phi})^{1/2}}, \tag{33}$$

a transformation can be found. Of course this approximation is only good when $\bar{\phi}/\bar{T}_e^*$ is large enough, which generally holds in the vicinity of the anode ($\bar{\phi} \approx 1$) when \bar{T}_e^* is small. For instance, consider the case of a SPT and a TAL operating at a typical $\phi_a = 300$ V. From Eq. (16) we have

$$(\bar{T}_e^*)_{BN} = 0.055, \quad \text{and} \quad (\bar{T}_e^*)_{SS} = 0.36, \tag{34}$$

and the corresponding curves for $F_1(\bar{\phi})$ are shown in Fig. 3.

It is clear from Fig. 3 that $F_2(\bar{\phi})$ is a good approximation for $F_1(\bar{\phi})$ for the SPT, especially near the anode ($\bar{\phi} \approx 1$). As \bar{T}_e^* increases, the point at which this approximation starts to depart from $F_1(\bar{\phi})$ recedes toward the anode. For the larger \bar{T}_e^* of the TAL ($\bar{T}_e^* = 0.36$) we should not expect the potential profile obtained from a solution obtained under this approximation to be valid, but the value of \bar{x}_{qn} should still give an approximation of the extent of the acceleration region since we expect, from the above-mentioned argument and Eq. (31), $\bar{\phi}_{qn}$ to be a good fraction of unity. We shall

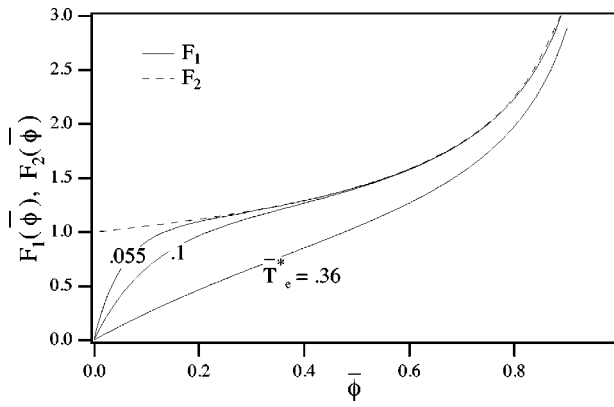


FIG. 3. Plot of $F_1(\bar{\phi})$ for three values of \bar{T}_e^* including those for boron nitride (SPT) and stainless steel (TAL) (in xenon at $\phi_a=300$ V). Also shown is the approximating function $F_2(\bar{\phi})$.

later estimate the error in our analytical approximation of \bar{x}_{qn} by comparing them to those obtained from a numerical solution of Eq. (28).

Keeping the extent of the validity of this approximation in mind, we proceed to find a solution Eq. (28) where $F_1(\bar{\phi})$ is replaced by $F_2(\bar{\phi})$,

$$\frac{d^2}{d\bar{x}^2} \left[2(1-\bar{\phi})^{1/2} + \frac{\bar{T}_e^*}{(1-\bar{\phi})^{1/2}} \right] + (1-\bar{\phi})^{-1/2} = 0. \quad (35)$$

By switching to the new variable Φ defined as

$$\Phi \equiv (1-\bar{\phi})^{1/2} + \frac{\bar{T}_e^*}{2(1-\bar{\phi})^{1/2}}, \quad (36)$$

the above-mentioned ODE is transformed into

$$2 \frac{d^2\Phi}{d\bar{x}^2} + F(\Phi) = 0, \quad (37)$$

where the function

$$F(\Phi) \equiv \frac{\Phi}{\bar{T}_e^*} + (\Phi^2 + 2\bar{T}_e^*)^{1/2} \quad (38)$$

does not contain any derivatives of Φ . This leads to

$$\left(\frac{d\Phi}{d\bar{x}} \right)^2 + \int F(\Phi) d\Phi = 0, \quad (39)$$

where the function $F(\Phi)$, given by Eq. (38), can be integrated to a closed form

$$\int F(\Phi) d\Phi = \frac{\Phi^2 - \Phi(\Phi^2 - 2\bar{T}_e^*)^{1/2}}{2\bar{T}_e^*} + \frac{\cosh^{-1}(\Phi)}{(2\bar{T}_e^*)^{1/2}} + C. \quad (40)$$

Here, C is the integration constant and is evaluated from the first boundary condition in Eq. (29) which, in terms of the new variable Φ , is

$$\frac{d\Phi}{d\bar{x}} = 0 \quad \text{at } \bar{x} = 0, \quad (41)$$

yielding

$$C = - \left[\frac{1 - (1 - 2\bar{T}_e^*)^{1/2}}{2\bar{T}_e^*} + \frac{\cosh^{-1}(1)}{(2\bar{T}_e^*)^{1/2}} \right]. \quad (42)$$

Finally, solving for $d\bar{x}$ in Eq. (39), integrating again, and applying the second boundary condition in Eq. (29) which, in terms of the new variable Φ , is

$$\Phi = 1 + \frac{\bar{T}_e^*}{2} \quad \text{at } \bar{x} = 0, \quad (43)$$

we find the solution we are seeking,

$$\bar{x} = \int_{\Phi}^{1+\bar{T}_e^*/2} d\Phi \left[- \frac{\Phi^2 - \Phi(\Phi^2 - 2\bar{T}_e^*)^{1/2}}{2\bar{T}_e^*} - \frac{\cosh^{-1}(\Phi)}{(2\bar{T}_e^*)^{1/2}} - C \right]^{1/2}. \quad (44)$$

To obtain the extent of the (quasineutral) acceleration region \bar{x}_{qn} , the lower bound in the above-mentioned integral must be changed to the value of Φ corresponding to $\bar{\phi}_{qn}$. From Eqs. (31) and (36) this lower bound is $2(\bar{T}_e^*/2)^{1/2}$, and we can write

$$\bar{x}_{qn} = \int_{2(\bar{T}_e^*/2)^{1/2}}^{1+\bar{T}_e^*/2} \frac{d\Phi}{[\dots]^{1/2}}. \quad (45)$$

The analytical expression of this integral is much too cumbersome to write and it is far easier to carry out the above-mentioned integration numerically with a simple quadrature.

There does exist a relatively compact closed form solution to the problem in the limit $\bar{T}_e^* \rightarrow 0$. Then, Eq. (39) becomes simply

$$\left(\frac{d\Phi}{d\bar{x}} \right)^2 + \int \frac{d\Phi}{\Phi} = 0, \quad (46)$$

and leads to

$$\bar{x} = \int_{\Phi}^1 \frac{d\Phi}{\sqrt{-\ln \Phi}}, \quad (47)$$

which in turn integrates to

$$\bar{x} = \int_{\Phi}^1 \frac{d\Phi}{\sqrt{-\ln \Phi}} = \frac{-\pi \text{Erfi}(\sqrt{\ln \Phi}) \sqrt{\ln \Phi}}{\sqrt{-\ln \Phi}}, \quad (48)$$

where

$$\text{Erfi}(z) = \frac{\text{Erf}(iz)}{i}. \quad (49)$$

The extent of the acceleration zone \bar{x}_{qn} , which for this particular case is the same as the anode position, \bar{x}_a , is obtained by changing the lower integration bound in the above-mentioned integral to 0.

TABLE I. Comparison of \bar{x}_{qn} estimates obtained using the approximate analytical solution to those obtained numerically.

\bar{T}_e^*	$\bar{\phi}_{qn}$	\bar{x}_{qn} (Runge-Kutta)	\bar{x}_{qn} (Analyt. Approx.)
0	1	1	1
0.05	0.972	0.842	0.848
0.1	0.95	0.766	0.757
0.36	0.82	0.468	0.37

C. Evaluation

We are now at a position to evaluate the extent of the (quasineutral) acceleration region \bar{x}_{qn} from the above-mentioned analytical solutions. The results for $\bar{T}_e^* = 0, 0.055$ (SPT with BN walls), 0.1, and 0.36 (TAL with SS walls) are tabulated in Table I where we also give the results of the direct numerical integration of the differential equation [Eq. (28)].

We note from Table I that the analytical approximations are good for the SPT ($\bar{T}_e^* = 0.055$) and for $\bar{T}_e^* = 0.1$ but underestimate x_{qn} by about 20% for the case of the TAL ($\bar{T}_e^* = 0.36$).

In light of the discussion of the approximation in Sec. III B, and of the plot in Fig. 3, we should expect this agreement to get worse as we get further downstream from the anode. Indeed this is shown by the potential profiles plotted in Fig. 4 where it is clear that while the analytical approximation of the *profile* is quite good for the SPT, it is not so for the TAL. However, the model, as we have seen in Table I, is better at estimating the *extent* of the zone, i.e., \bar{x}_{qn} , which is the focus of our study.

Before we discuss the implications of these results, it is informative to look at a set of potential profiles obtained from the direct numerical integration of the governing differential equation [Eq. (28)] over a wide range of \bar{T}_e^* values. These are shown in Fig. 5 along with the matching potential profile extensions in the space-charge-limited (nonquasineutral) sheath. These sheath solutions are beyond the domain of Eq. (28) since the model that led to that equation did not

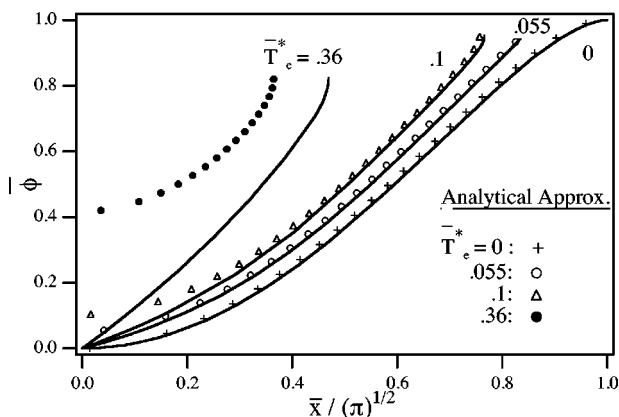


FIG. 4. Potential profiles obtained from the approximate analytical solution (scatter plot) compared to the profiles (line plot) obtained from the direct numerical integration of the differential equation [Eq. (28)], for four values of \bar{T}_e^* including those of the SPT (0.055) and the TAL (0.36).

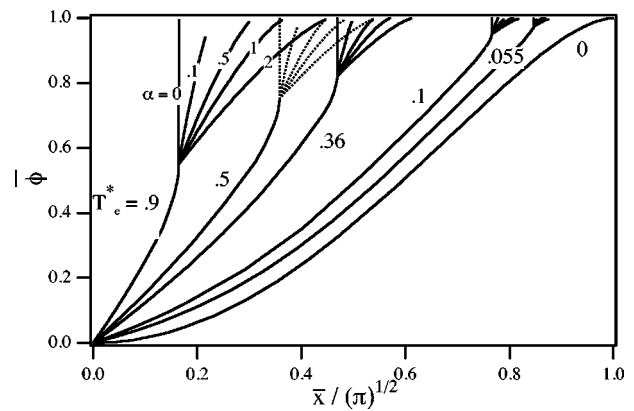


FIG. 5. Potential profiles obtained from the direct numerical integration of the differential equation [Eq. (28)], for a wide range of \bar{T}_e^* values including those of the SPT (0.055) and the TAL (0.36).

include Poisson’s equation. It is shown in Ref. 19 that in the anode sheath the potential distribution is determined by the ion space charge which, in the vicinity of the anode ($\bar{\phi} \approx 1$), leads to a Poisson equation in which the electron density can be neglected. Therefore, instead of Eq. (26) we can write¹⁹

$$\alpha \frac{d^2 \bar{\phi}}{d\bar{x}^2} = -(1 - \bar{\phi})^{-1/2}, \tag{50}$$

which leads to

$$\bar{x}_a - \bar{x} = \frac{2}{3} \sqrt{\alpha} (1 - \bar{\phi})^{1/2} \quad \text{for } \bar{x}_{qn} \leq \bar{x} \leq \bar{x}_a, \tag{51}$$

where

$$\alpha \equiv \frac{\nu_{iz}}{\nu_e} \frac{m_e \omega_{ce}^2 \epsilon_0}{e^2 n'}. \tag{52}$$

The corresponding sheath potential profiles are shown in Fig. 5 as extensions to the numerically obtained quasineutral profiles for a range of α values.

We note the following from that figure:

- (1) Wall properties have a significant effect on scaling the extent of the acceleration zone which is on the order of a few electron cyclotron radii.
- (2) With increasing \bar{T}_e^* (i.e., decreasing SEE coefficient) the total acceleration region (quasineutral plus sheath) becomes restricted to a thinner layer near the anode.
- (3) For the SPT, and even the TAL, the extent of the anode sheath (for $\alpha \leq 2$) remains a small portion of the extent of the total acceleration region, thus justifying the approximation $\bar{x}_{qn} \approx \bar{x}_a$ we adopted earlier when we used the extent of the quasineutral region (which is uniquely determined independently of α) as a measure of the extent of the entire acceleration region.
- (4) For both variants most of the the potential drop (97% for the SPT and 82% for the TAL) occurs in the quasineutral part of the acceleration region, implying that even the TAL is not truly a space-charge-sheath accelerator.

It may also be of interest to note that the above-presented model and results can conceivably be adapted to

study the effects of current-conducting walls (e.g., electrodes implanted in the acceleration region as in Refs. 27 and 28) by introducing the electron emission characteristics of such walls to the model through an effective \bar{T}_e^* .

D. Implications

Since the focus of our study is on the difference between the SPT and the TAL, we are compelled to explicitly estimate the magnitude of the reduction of the extent of the acceleration zone when the walls are changed from boron nitride to stainless steel, while other parameters, such as the magnetic field and the potential drop are kept constant (the latter at 300 V). From Table I we calculate a factor of 1.8 reduction in the *non-dimensional* extent. To calculate the actual dimensional reduction we write

$$\frac{(x_{qn})_{SPT}}{(x_{qn})_{TAL}} = \frac{(\bar{x}_{qn}l')_{SPT}}{(\bar{x}_{qn}l')_{TAL}} = \frac{(\bar{x}_{qn}\sqrt{\nu_e/\nu_{iz}})_{SPT}}{(\bar{x}_{qn}\sqrt{\nu_e/\nu_{iz}})_{TAL}}, \tag{53}$$

where we have used the definition of the characteristic length l' given in Eq. (21). The ratio ν_e/ν_{iz} can be approximated by the ratio of the respective cross sections Q_e/Q_{iz} , which is a function of the electron temperature. For the SPT and the TAL we have $T_e \approx T_e^* = 16.5$ and 107 eV, respectively, and the corresponding cross-sectional ratios for xenon can be calculated from the measurements in Refs. 29 and 30 to be

$$\frac{Q_e}{Q_{iz}} = 28 \text{ for } T_e = 16.5 \text{ eV (SPT)} \tag{54}$$

and

$$\frac{Q_e}{Q_{iz}} = 1.5 \text{ for } T_e = 107 \text{ eV (TAL)}. \tag{55}$$

Therefore

$$\frac{(x_{qn})_{SPT}}{(x_{qn})_{TAL}} \approx 2.3 \times \left(\frac{28}{1.5}\right)^{1/2} = 7.8. \tag{56}$$

The acceleration zone for the thruster with the metal (SS) walls is therefore confined to a region near the anode that is about eight times less in axial extent than that in the thruster with the insulator (BN) walls, thus justifying the appellation “thruster with anode layer” for the former.

IV. CONCLUDING PICTURE

The results obtained and the ensuing discussion allow us to draw a concluding idealized picture of the fundamental qualitative difference between the two variants of Hall thrusters. This picture is represented schematically in Fig. 6 where the SPT and TAL channels are shown along with the associated profiles of the potential ϕ , the electron temperature, T_e , and the wall potential ϕ_w ; the latter is based qualitatively on the calculations in Ref. 24.

As the electrons enter the channel (or are produced through volume ionization) their energy increases monotonically with the applied potential. With the increase in electron energy of the primaries comes an increase in the number of low-energy secondary electrons emitted from the walls. These electrons are represented by short and wide arrows

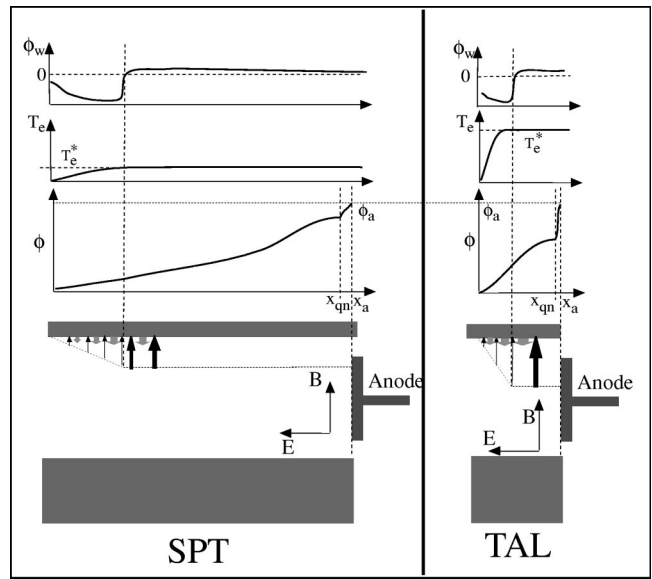


FIG. 6. Schematic of the idealized phenomenological picture illustrating the fundamental difference between the two Hall thruster variants.

(pointing away from the wall), whose width is representative of their numbers and whose height gives a qualitative measure of the secondaries’ energy (which is significantly lower than that of the primaries). The wall potential in that region, like in the standard case of a non-current-carrying wall in a plasma, is negative and repels electrons in order to keep the sum of the ion, primary electron, and secondary electron fluxes to zero. This situation continues upstream until a critical point is reached at which the number of emitted secondary electrons is large enough that the wall potential must revert in sign (and become electron attracting) in order to maintain the no-current condition. For the SPT, which has insulator walls, this happens at a relatively low electron temperature (16.5 eV for xenon gas and boron nitride walls), while for the case of TAL this does not happen until a much higher temperature since the secondary emission process for the metal is not as effective as that of the insulator.

Once this critical temperature, T_e^* , is reached the electron-attracting wall potential causes a substantial increase in the electron heat flux to the walls thereby short-circuiting any further increase in T_e . In our idealized model, this is represented by an electron energy profile that asymptotes to T_e^* [cf. Eq. (17) and the qualitative T_e plots in Fig. 6].

So far all is happening under conditions of quasineutrality. Since the ion flux is constant but the ion velocity is lower as we approach the anode, and since the electron temperature stopped increasing (due to the quenching effect described earlier), the electron density must increase in that direction in order to maintain quasineutrality [cf. Eq. (8)]. This will eventually lead to a crisis since further increase in electron density must be compensated by further increase in the electric field, $d\bar{\phi}/d\bar{x}$, in order for the electron current not to vanish. This can be seen by recalling Eq. (24),

$$\bar{j}_{e_x} = \bar{n}_e \frac{d\bar{\phi}}{d\bar{x}} - \bar{T}_e^* \frac{d\bar{n}_e}{d\bar{x}}, \quad (57)$$

where we have taken \bar{T}_e^* as a constant and moved it outside the derivative. At a critical value of the potential near the anode, the electric field would have go to infinity [cf. Eq. (30)]; this is indicative of the failure of the quasineutral description at that axial location which is denoted by x_{qn} in Fig. 6.

For the SPT, the vigorous SEE processes lead to a lower quenching temperature for the electrons (as discussed previously) and since the latter scales the magnitude of the pressure gradient [cf. the second term on the right-hand side of Eq. (57)], the required increase in the electric field is delayed until a larger portion of the potential is reached upstream [sepcifically, until $\bar{\phi} = 1 - \bar{T}_e^*/2$, cf. Eq. (31)]. This relaxation on the requirement for electric field increase implies that the potential is more spatially relaxed compared to the case where the quenching temperature is high (TAL). The acceleration zone is therefore more spatially extended for the SPT.

Finally, it must be cautioned that while the plots of the nondimensional profiles in Fig. 5 show a more extended *non-dimensional* sheath region for the TAL as compared to the SPT case, the opposite is true for the *dimensional* extent due to the scaling of the ratio of the relevant cross sections with the electron temperature as discussed in Sec. IIID in the context of the quasineutral extent. Therefore, the sheath axial extent for the TAL is shown graphically in Fig. 6 to be smaller than that of the SPT. While the sheath extent is smaller for the TAL, a relatively larger portion of the potential drop occurs in the TAL's anode sheath as also shown graphically in Fig. 6.

ACKNOWLEDGMENTS

The author acknowledges the assistance of K. Polzin, S. Spektor, and K. Sankaran. He is also thankful for insightful discussions with Professor S. H. Lam to whom this paper is dedicated on the occasion of his retirement.

¹G. Seikel and E. Reshotko, *Bull. Am. Phys. Soc.* **7**, 414 (1962).

²F. Salz, R. G. Meyerand, and E. C. Lary, *Bull. Am. Phys. Soc.* **7**, 441 (1962).

³E. Lary, R. Meyerand, and F. Salz, *Bull. Am. Phys. Soc.* **7**, 441 (1962).

⁴G. L. Cannes and G. L. Marlotte, *AIAA J.* **2**, 1234 (1964).

⁵C. B. E. A. Pinsley and C. Banas, *J. Spacecr. Rockets* **1**, 525 (1964).

⁶C. O. Brown and E. A. Pinsley, *AIAA J.* **3**, 853 (1965).

⁷G. James and R. S. Lowder, *Phys. Fluids* **9**, 1115 (1966).

⁸D. L. Chubb and G. R. Seikel, *Basic Studies of a Low Density Hall Current Ion Accelerator* (AIAA, Washington, DC, 1966), AIAA-66-76.

⁹H. Kaufmann, *AIAA J.* **23**, 78 (1985).

¹⁰E. Y. Choueiri, *Phys. Plasmas* **8**, 1411 (2001).

¹¹A. I. Morozov, A. Y. Kislov, and I. P. Zubkov, *JETP Lett.* **7**, 211 (1968).

¹²M. Martinez-Sanchez and J. Pollard, *J. Propul. Power* **14**, 688 (1998).

¹³J. Brophy, J. Barnett, J. Sankovic, and D. Barnhart, *Performance of the Stationary Plasma Thruster: SPT-100* (AIAA, Washington, DC, 1992), AIAA-92-3155.

¹⁴R. X. Meyer, *A Space-Charge-Sheath Electric Thrustor* (AIAA Washington, DC, 1966), AIAA-66-927.

¹⁵R. X. Meyer, *Acceleration of Cesium Ions by Means of a Negative Space Charge Sheath* (AIAA, Washington, DC, 1966), AIAA-66-256.

¹⁶R. X. Meyer, *AIAA J.* **5**, 2057 (1967).

¹⁷R. X. Meyer, *J. Spacecr. Rockets* **7**, 251 (1970).

¹⁸S. Grishin and L. Leskov, *Electric Propulsion for Space Vehicles* (in Russian: *Elektricheskie Raketye Dvigateli Kosmicheskikh Apparatov*) (Mashinostroenie, Moscow, 1989).

¹⁹A. Zharinov and Y. S. Popov, *Sov. Phys. Tech. Phys.* **12**, 208 (1967).

²⁰A. Dekker, *Solid State Phys.* **6**, 251 (1968).

²¹A. Sommer, *McGraw-Hill Encyclopedia of Physics* (McGraw-Hill, New York, 1983), pp. 1026–1029.

²²A. Modinos, *Field, Thermoionic, and Secondary Electron Emission Spectroscopy* (Plenum, New York, 1984).

²³A. Morozov, Y. V. Epsinchuck, G. N. Tilinin *et al.*, *Sov. Phys. Tech. Phys.* **17**, 38 (1972).

²⁴J. Fife, M. Martinez-Sanchez, and J. Szabo, *A Numerical Study of Low-Frequency Discharge Oscillations in Hall Thrusters* (AIAA, Washington, DC, 1997), AIAA-97-3052.

²⁵J. Bugeat and C. Koppel, *Development of a Second Generation of SPT* (The Electric Rocket Propulsion Society, Worthington, OH, 1995), IEPC-95-35.

²⁶*Atomic Data for Fusion*, edited by E. W. Thomas (Oak Ridge National Laboratory, Oak Ridge, TN, 1985), Vol. 3.

²⁷N. Fisch, Y. Raitse, A. Litvak, and L. Dorf, *Design and Operation of Hall Thruster with Segmented Electrodes* (AIAA, Washington, DC, 1999), AIAA-99-2572.

²⁸A. Fruchtman, N. J. Fisch, and Y. Raitses, *Phys. Plasmas* **8**, 1048 (2001).

²⁹A. Brown, *Basic Data of Plasma Physics* (McGraw-Hill, New York, 1959).

³⁰Y. K. Kim, J. P. Santos, and F. Parente, *Phys. Rev. A* **62**, 052710 (2000).